Particle manipulation in Hele-Shaw flow with programmable hydrodynamics

Kislaya, Ankur; Samant, Aniket Ashwin; Veenstra, Peter; Tam, Daniel S.W.; Westerweel, Jerry

DOI
10.1063/5.0251563

Publication date
2025

Document Version
Final published version

Published in
Physics of Fluids

RESEARCH ARTICLE | MARCH 05 2025

Particle manipulation in Hele–Shaw flow with programmable hydrodynamics

Ankur Kislaya ; Aniket Ashwin Samant ; Peter Veenstra; Daniel S. W. Tam ; Jerry Westerweel

Physics of Fluids 37, 032012 (2025)
https://doi.org/10.1063/5.0251563

Physics of Fluids ARTICLE pubs.aip.org/aip/pof

Particle manipulation in Hele–Shaw flow with programmable hydrodynamics

Cite as: Phys. Fluids **37**, 032012 (2025); doi: 10.1063/5.0251563
Submitted: 3 December 2024 · Accepted: 3 February 2025 ·
Published Online: 5 March 2025

Ankur Kislaya,[1] Aniket Ashwin Samant,[2] Peter Veenstra,[3] Daniel S. W. Tam,[1,a)] and Jerry Westerweel[1]

AFFILIATIONS

[1]Laboratory for Aero and Hydrodynamics, Delft University of Technology, Mekelweg 2, 2628 CD Delft, The Netherlands
[2]Faculty of Electrical Engineering, Mathematics and Computer Science, Delft University of Technology, Mekelweg 4, 2628 CD Delft, The Netherlands
[3]Shell Technology Centre Amsterdam (STCA), Grasweg 31, 1031 HW Amsterdam, The Netherlands

[a)]Author to whom correspondence should be addressed: D.S.W.Tam@tudelft.nl

ABSTRACT

This paper presents a microfluidic approach that dynamically controls the hydrodynamic flow and the streamlines to enable complex multi-particle manipulations within a single device. The approach combines the design of a flow-through microfluidic Hele–Shaw flow cell together with an optimization procedure to find *a priori* optimal particle pathlines, and an effective proportional–integral–derivative (PID) feedback controller to provide real-time control over the particle manipulations. In the device, particles are manipulated with hydrodynamic forces, by using a uniform flow through the flow cell and three inlets perpendicular to the flow cell. The streamlines within the device are manipulated by injecting or extracting fluid through the three inlets. The Hele–Shaw geometry allows a fast and accurate prediction of the particle trajectory, meaning only a simple PID controller is required to correct for particle deviations. The robustness of this approach is demonstrated by implementing multiple functions within the device, including particle trapping, particle sorting, particle separation, and assembly. The real-time control procedure affords accurate particle manipulation, with a maximum error on the order of the diameter of the particle.

I. INTRODUCTION

Current microfluidic devices are typically designed for single applications and are tailored for a specific task or manipulation activity. This approach leads to microfluidic devices with fixed designs and channel configurations. Microfluidic applications, on the other hand, often require dynamic manipulations involving particle trapping, separation, assembly, or sorting. Such particle manipulation in microfluidics represents a challenge in devices with static channel configurations and is performed using various contact techniques relying on micro-channel geometry and non-contact techniques using lasers, magnetic fields, acoustic forces, electrical fields, and hydrodynamic forces.[1–6] Particle and droplet manipulation within microfluidic devices has been achieved with passive and active techniques. Passive techniques use the geometry and topology of the micro-channel to perform the manipulation activity. In contrast, active manipulation relies on the interactions between particles with external forces and fields, which strongly depend on the physical properties of the particle, droplet, or cell being manipulated. These properties include electrical properties, chemical composition, acoustic properties, or refractive index. These strong interactions are particle dependent and may not always be compatible with sensitive biological samples.[7]

An attractive alternative to using strong physical fields and interactions is to manipulate and trap micro-particles by directly controlling the direction of the flow field on the particle scale and to precisely manipulate the streamlines of the flow.[7] Theoretical work has demonstrated the feasibility of performing complex particle manipulation through flow control in a simple device.[8] By varying the flow rates through a seven-channel device, flow fields can be used to assemble particles into predetermined structures.[8] Experimental realizations of these hydrodynamic methods for particle trapping and manipulation have been implemented. Automated four-channel cross-slot devices have been developed to confine single particles in the device.[9–12] A six-channel device was designed to generate the so-called Stokes traps and was used to trap simultaneously two particles in two separate stagnation points and manipulate their path,[13] to control particle using flow patterns[14] and to control the orientation of anisotropic particles.[15] Similar approaches have been used to guide the flow of a reagent inside a microfluidic flow cell along a re-configurable trajectory.[16] Recent

interest into devices with open volume confinements has created new opportunities for fluid manipulation, enabling the development of reconfigurable microfluidic devices that dynamically adjust shape and function for real-time experimentation and decision-making.[17,18] Non-hydrodynamic methods often involve the use of external fields such as magnetic, acoustic, and electric fields, requiring complex control mechanisms and involving interactions between physical fields and particle properties.[19] In contrast, hydrodynamic forcing offers a simpler, non-contact alternative for manipulating and trapping microparticles.[20,21] The microfluidic devices that support reconfigurable trajectory have advantage of rapid prototyping and quick modifications to optimize the desired outcome.[22]

In this work, we present a microfluidic approach to achieve the dynamic control of particle pathlines within a flow-through microfluidic device. These particle manipulations rely on precise control of the hydrodynamic flow on the micrometer scale. We implement this approach in a microfluidic device with no physical channels and channel junctions, and instead, we directly use the flow field to guide the flow of particles in "virtual channels" or to trap particles at hydrodynamic stagnation points. We use a three-dimensional (3D) printed rectangular channel geometry, with integrated inlet/outlet ports to closely reproduce ideal Hele–Shaw flow conditions. Our flow cell geometry is key to generating Hele–Shaw flows in very close agreement with direct flow simulations using potential flow theory. This allows us to pre-compute complex particle manipulations at very low computational costs, and the corrections of the particle position during an experiment only require a simple controller, because the deviations between the predicted and measured trajectories are minimal. Here, we present our approach, which combines three key aspects: (1) the design of a flow-through microfluidic flow cell in a Hele–Shaw geometry, with the ability to manipulate the streamlines of the flow; (2) an optimization procedure to find *a priori* optimal particle path-lines; and (3) a *proportional-integral-derivative* (PID) feedback controller for real time control of particle manipulations.

First, the microfluidic device is a Hele–Shaw cell, where "virtual channels" are generated by a uniform flow in the flow chamber and three ports perpendicular to the flow chamber. These three ports can inject into or extract fluid from the flow cell to deviate the streamlines in the middle of the flow chamber and allow us to integrate multiple functionalities such as particle trapping and separation onto a single device. Modulating the volumetric flow rates through the three ports enables manipulation of the streamlines in devices with different geometries toward particle manipulation.

The Hele–Shaw flow cell with inlet/outlet ports is 3D printed as a single solid piece to ensure the orthogonality of the inlets with the main flow direction and the axisymmetry of the inlet. This requirement is necessary for the flow through the inlet/outlet ports to closely reproduce the radial velocity fields induced by a source or a sink in potential flow. The strength of a source/sink in potential flow is characterized by the volumetric flow rate, which we closely control in our experiments by using pressure pumps with integrated flow meters. Our Hele–Shaw geometry with inlet/outlet ports achieves excellent agreement between the streamlines computed using a reduced base numerical potential flow solver and the streamlines recorded experimentally.

Second, the flow rates required for a specific particle manipulation are determined *a priori* using a two-step optimization procedure based on the reduced base potential flow solver. Proof of concept uses a simple semi-analytical numerical model and allows real-time prediction of the streamline pattern within the flow cell. The optimal particle trajectory is determined to minimize the flow rates through the three inlet/outlet ports and to minimize time variations in the flow rates. This optimization routine is called *a priori* particle manipulation algorithm. Finally, a closed loop feedback control scheme is implemented to mitigate the experimental error (such as surface roughness, particle density, and off-center particle position along the channel height) to achieve robust and repeatable experimental results for various experiments. Our microfluidic device closely reproduces the streamline pattern predicted by the potential flow solver and the precomputed particle trajectories, hence minimizing the requirements for the feedback controller. In our setup, a simple PID controller is enough to efficiently correct for particle deviations.

During an experiment, the error in particle position can be determined relative to the *a priori* optimized trajectory, and additional flow rates are applied to correct for the error. Thus, we use a combination of the *a priori* particle manipulation algorithm and the PID feedback loop to achieve the desired particle path. The results show that experimentally determined particle positions closely agree with the optimized trajectory, with the maximum error at the end of the manipulation being on the order of the particle diameter. The present system is designed for proof-of-principle purposes, with an intentional focus on flexibility rather than fast performance. Increase in speed and overall throughput can be achieved by using high-speed imaging and dedicated hardware.

II. DEVICE DESIGN AND PARTICLE MANIPULATION ALGORITHM

We first present a description of the Hele–Shaw flow cell, the experimental method, and the flow control strategies. For a more detailed description, the reader is referred to Ref. 23.

Microfluidic Hele–Shaw device and "virtual channels." The geometry of the flow cell is designed to generate streamline patterns, reminiscent of well characterized flows in potential flow theory. The flow cell is designed in this way to support the rapid online computation of streamline patterns, which is required to control the particle. A schematic of all the essential components for the experiment is displayed in Fig. 1(b). The Hele–Shaw cell (length $l = 40$ mm, width $w = 12$ mm, and height $h = 350\ \mu$m) in Fig. 1(d) is a 3D printed device made from clear resin using a 3D printer (Formlabs FORM 3). Inlet/outlet ports 1, 2, and 3 are located at coordinates (3.5 mm, 2.5 mm), (9 mm, 6 mm), and (3.5 mm, 9.5 mm), respectively, from the bottom left corner of the region of interest. Images are recorded with a sCMOS camera (PCO) with a pixel pitch of 6.5 μm. The camera is mounted on a microscope (Nikon Eclipse Ti) with a 1 × objective. The acquisition frequency is 5 Hz, corresponding to an average in-plane displacement of 2–3 pixels between two consecutive recordings. The coordinates of the particles during the experiment are acquired using an in-house developed LabVIEW program that is used to acquire the images. The setup consists of a pressure pump (Fluigent MFCS-EZ) that regulates the pressure in five pressure ports. These ports are connected to five reservoirs that contain the working fluid. The working fluid used in all the experiments is de-ionized water. These five reservoirs are connected to a flow sensor that measures the volumetric flow rates, Q_i, where i corresponds to the inlet/outlet ports as shown in Fig. 1(b). The resolution of the pressure controller is 20.7 μ bar, which corresponds approximately to 0.2 μl/min. For reservoir 4, an additional

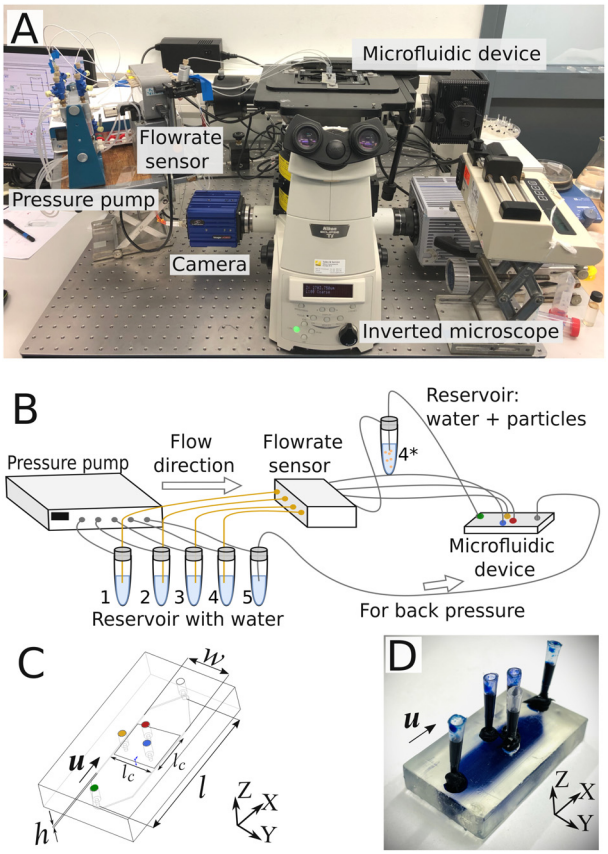

FIG. 1. (a) Experimental setup with all required components. (b) Schematic of the experimental setup showing the microfluidic device connected to reservoirs through a flow rate sensor. A pressure pump drives the fluid through the reservoirs using pressurized air. Reservoirs 1, 2, and 3 correspond to ports 1, 2, and 3, respectively. Reservoir 4 is connected to an additional reservoir 4* containing particle solution. Reservoir 4* is connected to the uniform flow inlet. Reservoir 5 is attached to the outlet of the microfluidic device. The flow is regulated using an in-house developed LabVIEW program. (c) Schematic of the microfluidic device with channel length l, width w, and height h. The uniform flow is denoted as $\mathbf{u}$. The flow is parabolic over the channel height in the Z direction. The circles represent uniform-flow inlet (filled green circle), inlet/outlet ports 1 (filled blue circle), 2 (filled red circle), and 3 (filled yellow circle). The region of interest, where particle manipulation occurs, is a square region denoted by l_c. (d) The actual 3D printed microfluidic device filled with methylene-blue/water solution to visualize the flow channel.

reservoir 4* is connected to the device further downstream of the flow sensor. This is done to avoid any contamination and clogging of the capillaries in the flow sensor from the particles to be manipulated. Polystyrene fluorescent microspheres (density: 1 g/cm^3) with a mean diameter of 212 μm (Cospheric) are used as the target particles. For the pollen trapping experiment, dry conifer pollen grains with a mean diameter of 70 μm are used. They have a density of about 1 to 1.15 g/cm^3, but they absorb water so that their actual density is close to 1 g/cm^3 and nearly neutrally buoyant. At the final outlet corresponding to the fifth reservoir, a back pressure of 2.5 kPa is imposed to allow net-negative flow. The coordinates of the particles during the experiment are acquired and tracked with LabVIEW.

Simultaneous manipulation of N particles requires a minimum of $2N+1$ inlets, i.e., $2N$ for movement in X and Y positions and an additional channel to satisfy mass conservation.[8] Thus, for $N=2$, at least five ports are required. A schematic of the microfluidic device, which has an inlet for continuous uniform flow, three ports to inject/extract fluid, and an outlet, is illustrated in Fig. 1(c). We consider laminar flow, $\mathbf{u}$, between the two parallel plates, i.e., a Hele–Shaw flow.[24] The Hele–Shaw condition is valid when the in-plane length of the flow domain l is much larger than the channel height h, i.e., $l \gg h$. Under the Hele–Shaw flow condition, the velocity profile is parabolic in the wall-normal direction (Z direction) with a no-slip condition at the upper and lower walls. Integrating the Navier–Stokes equation along the Z direction yields a governing equation for the depth-averaged velocity, which is identical to Darcy's law. The mean flow, with components (u,v) in the (X,Y) plane, is a potential flow, where the flow potential is the pressure and satisfies the Laplace equation.[25] The Hele–Shaw approximation breaks down near boundaries when the distance to the boundary becomes of the order of the plate distance h. As the Laplace equation is linear, flow fields can be written as a linear superposition of known potential flow solutions, such as sources and sinks.[25] This method is implemented in a numerical efficient 2D discrete source-based panel method,[26] which we use to compute a solution for the depth averaged flow velocity in the aft-part of the microfluidic device; for further details, see (Ref. 23, Sec. 3.2.3).

Non-dimensionalization. All length scales are non-dimensionalized using the characteristic length scale of the region of interest, $l_c = 12$ mm as shown in Fig. 1(c). We further use the characteristic uniform flow $\mathbf{u}_c = (u_c,0)$ to non-dimensionalize the flow rates Q_i and the characteristic timescale $t_c = l_c/\mathbf{u}_c$. A non-dimensional uniform flow $\mathbf{u}^* = (u^*, 0)$ is defined by the user. The non-dimensional parameters are defined as follows:

$$X^* = \frac{X}{l_c}, \quad Y^* = \frac{Y}{l_c}, \quad Z^* = \frac{Z}{l_c}, \tag{1}$$

$$l^* = \frac{l}{l_c}, \quad h^* = \frac{h}{l_c}, \quad w^* = \frac{w}{l_c}, \quad Q_i^* = \frac{Q_i}{l_c^2} \cdot \frac{u^*}{u_c}, \tag{2}$$

with $i = 1, 2, 3$ representing the three ports. Here, X, Y, and Z represent the dimensional length scale, and X^*, Y^*, and Z^* represent the associated non-dimensionalized length scale. l, w, and h are dimensional length, width, and height of the flow cell and l^*, w^*, and h^* the related non-dimensional length, width, and height of the flow cell; $\mathbf{Q} = [Q_1, Q_2, Q_3]$ are dimensional flow rates corresponding to inlet/outlet ports 1, 2, and 3, respectively, while $\mathbf{Q}^* = [Q_1^*, Q_2^*, Q_3^*]$ are the corresponding non-dimensional flow rates. The non-dimensionalized parameters of the flow cell are used extensively in the calculation of the optimized particle trajectory using the *a priori* particle manipulation algorithm. The dimensional values of the flow rates are deduced from the non-dimensional ones by fixing the characteristic background flow velocity u_c. This velocity determines the timescale of the manipulation and is chosen such that the flow rate inputs remain within the limits of the pump and flow controllers. The main limitation in our set up is related to the response time of the pump required to ensure accurate pressure pump resolution. The response time of the pump is characterized in this work by analyzing the step response to the system. We find that our pump has a response time of 2.5 s. The details of these experiments can be found in the supplementary material, 1. Modeling the response time of the pump.

Particle-path optimization. The effectiveness of the optimization procedure crucially depends on the rapid computation of the streamline patterns. In the following, we describe the workflow of the *a priori* particle manipulation algorithm, which computes the time-dependent flow rates $\boldsymbol{Q}$ corresponding to the optimal particle trajectories between the initial particle position $\boldsymbol{X}_{Pi}(t_0)$ and the final particle position $\boldsymbol{X}_{Pi}(t_f)$. Here, i is the index of the particle to be manipulated, while t_0 and t_f represent the times where the particle is at the initial position and the final position, respectively. The *a priori* particle manipulation algorithm is designed to minimize both the magnitude of the flow rates $\boldsymbol{Q}$ and the magnitude of the flow rate variations $(d\boldsymbol{Q}/dt)$. This ensures simple inputs to the pump for better control over the flow rates during the experiments. In this approach, we assume that the particles are sufficiently large ($d_p \approx h$) such that their motion is not affected by Brownian motion. Hence, the particle is advected at the local fluid velocity $\mathbf{u}(\boldsymbol{X}_{Pi})$, such that $\dot{\boldsymbol{X}}_{Pi}(t) = \eta \cdot \mathbf{u}(\boldsymbol{X}_{Pi})$, where $\boldsymbol{X}_{Pi}(t)$ is the particle position in the X and Y directions at time t, i the index of the particle to be manipulated, and η a proportionality constant that depends on the particle shape and ratio of particle size to channel height.[27] Here, the particles used for the experiments are spherical and have a particle diameter-to-channel height ratio of 0.6 with $\eta = 0.88$.

For the particle-path optimization, we develop a reduced-order, semi-analytical computational approach. To decrease the complexity of the optimization problem, we optimize the flow rates $\boldsymbol{Q}^*(t) = [Q_1^*(t), Q_2^*(t), Q_3^*(t)]$ as a function of time, instead of optimizing for a discrete set of values of the flow rates. The time-varying flow rates are projected onto a finite base of orthogonal polynomials, and the coefficients of those orthogonal expansions are used as design variables. The total time duration for optimization, t^* is defined over a range [a,b] where a given polynomial weight function satisfies orthogonality. A time interval $t^* = [-1, 1]$ is chosen because most of the orthogonal polynomials relevant to this study have their orthogonality relation in the range $[-1, 1]$.

The optimization is performed in two steps: the first step finds a feasible solution, while the second optimization step refines the solution to minimize both the magnitude of the flow rates and the time variation of the flow rate. Figure 2(a) shows a flow chart of the two-step optimization process. Figures 2(b)–2(e) shows computed flow rates for non-optimized and optimized particle trajectories.

A. First optimization step: Unconstrained optimization

The input parameters for the first optimization step are the initial particle position $\boldsymbol{X}_{Pi}(t_0^*)$, the pre-defined final particle position $\boldsymbol{X}_{Pi}(t_f^*)$, and the non-dimensional uniform flow $\boldsymbol{u}^* = (u^*,0)$. The optimization algorithm uses the coefficients of the orthogonal expansions to compute the flow rates that yield an optimized particle trajectory between pre-defined initial and final particle position. A quasi-Newton method[28] based unconstrained optimization is used to minimize the objective function J_1, which is defined as the distance between the particle position at the final time step $\boldsymbol{X}_{Pi}(t_k^*)$ and the pre-defined final position $\boldsymbol{X}_{Pi}(t_f^*)$,

$$\min_{\boldsymbol{Q}^*} J_1 = ||\boldsymbol{X}_{Pi}(t_k^*) - \boldsymbol{X}_{Pi}(t_f^*)||. \tag{3}$$

This first step yields a particle trajectory, which reaches the target final position.

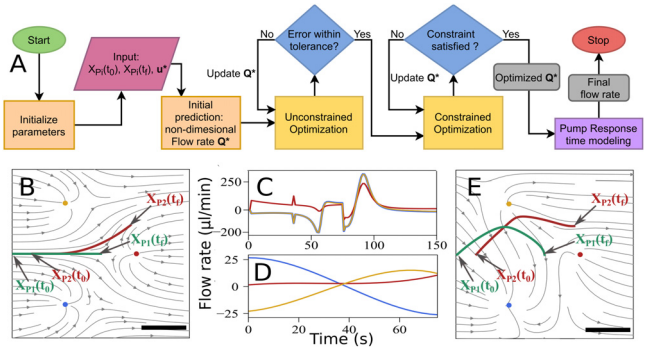

FIG. 2. (a) Overview of the *a priori* particle manipulation algorithm. (b) and (e) depict particle separation, where the trajectories of two particles are controlled from their initial position to their respective final desired positions. The pre-defined initial and final particle locations are defined as $\boldsymbol{X}_{P1}(t_0)$ and $\boldsymbol{X}_{P1}(t_f)$ for particle 1 and $\boldsymbol{X}_{P2}(t_0)$ and $\boldsymbol{X}_{P2}(t_f)$ for particle 2. Achieving the non-optimized trajectory in (b) requires higher flow rates with higher flow rate fluctuations (c) compared to the flow rate required (d) for the optimized particle trajectory (e). The scale bar represents 4 mm.

B. Second optimization step: Constrained optimization

The $\boldsymbol{Q}^*$ and the particle trajectory obtained from the first optimization step are used as the input parameters for the second optimization step. This second optimization step uses a gradient descent-based constrained optimization, where the objective function J_2 to be minimized consists of two components: the variations in flow rate $\frac{d\boldsymbol{Q}^*}{dt^*}$ and the absolute value of the flow rates $\boldsymbol{Q}^*$. The objective function J_2 is minimized subject to the constraint that the distance between the particle position at the final time step $\boldsymbol{X}_{Pi}(t_k^*)$ and the pre-defined final position $\boldsymbol{X}_{Pi}(t_f^*)$ is minimal

$$\min_{\boldsymbol{Q}^*, \frac{d\boldsymbol{Q}^*}{dt^*}} J_2 = \alpha \cdot \int_{t^*=-1}^{t^*=1} \frac{\partial |\boldsymbol{Q}^*|}{\partial t^*} dt^* + \beta \cdot \int_{t^*=-1}^{t^*=1} |\boldsymbol{Q}^*| dt^*, \tag{4}$$

such that the following constraint is imposed:

$$||\boldsymbol{X}_{Pi}(t_k^*) - \boldsymbol{X}_{Pi}(t_f^*)|| = 0. \tag{5}$$

Here, α and β are arbitrary weights that can be tuned based on the flow rates, $\boldsymbol{Q}^*$, to emphasize either small-time variations (when α is comparatively higher) or small absolute values (when β is higher). Constant values of 1 and 10^{-3} are used for α and β, respectively. These values are used to prioritize the minimization of the flow rate variations. The integrals in Eq. (4) are numerically estimated using the trapezoidal rule. The dimensions are applied to the non-dimensional flow rates $\boldsymbol{Q}^*$ using the characteristic length scale l_c and the characteristic uniform flow $\boldsymbol{u_c}$. The dimensional flow rate is denoted as $\boldsymbol{Q} = [\boldsymbol{Q_1}, \boldsymbol{Q_2}, \boldsymbol{Q_3}]$ for inlet/outlet ports 1, 2, and 3, respectively.

The *a priori* particle manipulation algorithm uses a linear combination of the coefficients of the orthogonal polynomials. A parametric study is carried out to investigate which orthogonal polynomials are best suited for this study; see (Ref. 23, Sec. 3.4.3). Polynomials such as Legendre polynomials, Chebyshev polynomials of the first kind, and Hermite polynomials are investigated. The choice of orthogonal polynomials is a mathematical choice and not a physics-based, because all three sets of polynomials give an optimal solutions. In practice, we find

that the convergence of Hermite polynomials to the optimal solution is slower compared to Legendre and Chebyshev polynomials. The performances of the Legendre and Chebyshev polynomials are very similar and converge to the same optimized particle trajectories and flow rate bounds. Nevertheless, Legendre polynomials are selected as a suitable candidate for the *a priori* particle manipulation algorithm, because in practice they show the lowest flow rate variations. The pre-defined flow rates from the *a priori* particle manipulation algorithm are transmitted to the pressure pump as discrete input points. However, the volumetric flow rate imposed by the pump does not reach the desired flow rate values instantaneously, because the pump responds with a finite time delay. In order to take into account this systematic error from the pump, the pump response time is computed; see also (Ref. 23, Sec. 3.3).

Closed-loop feedback control. The *a priori* manipulation algorithm leverages the linearity of potential flow theory to determine the optimized particle trajectory strategy in a fast, straightforward, and efficient manner. However, the *a priori* particle manipulation algorithm has a few limitations. Effects such as surface roughness and off-center particle position in the channel are not accounted for. To address these limitations, the *a priori* particle manipulation algorithm is coupled with closed-loop control, which allows improved control of the particle in an experiment. In general, a closed-loop control system is a system of hardware and software that can automatically adjust variations in a process to a set point with pre-defined limits without human interaction. In our case, we use a proportional–integral–derivative (PID) controller that provides corrective flow rates to the inlet/outlet ports based on the position error of the particles. The particle position error is defined as the difference between the particle location from the *a priori* manipulation algorithm and the experimentally measured particle location. A step-by-step description of how the positional error is measured and corrected in real-time, along with a visual flow chart, is provided in the supplementary material (supplementary material, 2. Working principle of PID controller). The performance and robustness of the PID controller in response to inputs deviating from ideal inputs are characterized *in silico* by introducing noise in the flow rates, up to 5 μL/min. We use these simulations to fine-tune the controller's gain constants. In experiments, the PID controller successfully manipulated elliptical-shaped particles, such as conifer pollen. It performed optimally as long as the particles remained suspended in the flow. However, when particles adhered to the upper or lower walls, the controller began to issue large corrective inputs, ultimately leading to the failure of the experiment; for further details, see (Ref. 23, Sec. 4.3).

III. RESULTS

Flow validation in the Hele–Shaw cell To validate our approach, we first compare the flow field generated in our device with numerical simulations. We begin by validating our numerical approach by comparing the flow fields computed using the panel method with the flow field computed using COMSOL simulations by solving the full Navier–Stokes equations; details are provided in (Ref. 23, Sec. 3.2.4). We find our reduced base potential solver to be in excellent agreement with our COMSOL simulations. The agreement between the potential flow and the COMSOL simulations demonstrates that the inertial terms of the Navier–Stokes equations, as well as the effects of lateral boundaries, can be neglected under the Hele–Shaw condition ($l \gg h$) and when the distance to the wall exceeds h.

Next, we compare our numerical simulations with experimental results. For this, we choose a flow configuration corresponding to a uniform flow superposed with a single source. Experimentally, we keep the volumetric flow rate for the uniform flow constant, and impose the volumetric flow rate through a single inlet. The streamline pattern corresponding to this flow is a Rankine half body and is characterized by the presence of a stagnation point upstream of the inlet;[25] see Fig. 3(b). We find the streamlines measured experimentally to be in agreement with the computed streamlines, see Figs. 3(a) and 3(b). We quantify the agreement by recording the location of the stagnation point for an increasing value of the flow rate through the inlet. The potential flow model is validated by comparing the position of a stagnation point induced by a single source in a uniform flow. We measure the location of the stagnation point in the flow chamber. The stagnation point is inherently unstable because it is sensitive to the system setup, such as the geometry of the flow cell, small flow rate variations and the placement of the inlet port. Small changes in these factors can cause the stagnation point to move unpredictably. The agreement between the location of the stagnation point computed with the panel method and both the location computed using COMSOL simulations and the location measured in our experiments indicates that the flow field computed by the panel method accurately represents the actual flow field. The stagnation point from the experimental data set is determined from the measured streamlines using Psi-PIV.[29] The experimentally determined stagnation point is a statistical average over 500 images to yield a properly converged estimation. For a more comprehensive understanding of the Psi-PIV workflow and streamline extraction, please refer to the Psi-PIV journal paper.[29] Figure 3(a) presents a good agreement between results from the panel method, COMSOL, and the experiments for the spatial location of stagnation point for increasing source strength. There are no fitting parameters in this figure, and the flow rates are direct inputs in both the simulation and the experiments. This demonstrates that the panel method accurately predicts the streamlines of the flow in the Hele–Shaw device. It also validates the design of our finite-size ports to closely reproduce axisymmetric radial flow of an ideal source. The panel method is computationally inexpensive compared to COMSOL, since the former is strictly based on potential flow theory, whereas the latter solves the Navier–Stokes equations. This makes it the method of choice for fast online computations, which are required within our feedback control loop.

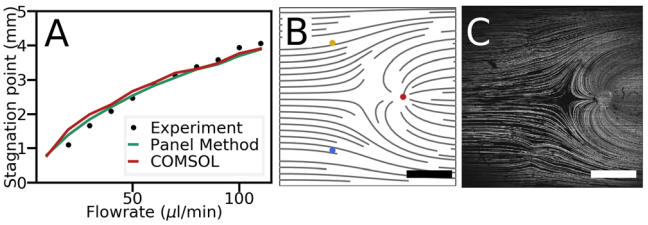

FIG. 3. (a) Comparison between the source-based panel method, COMSOL simulations, and experiments to characterize the device in terms of the location of the stagnation point of the Rankine half-body flow. The Rankine half-body strength was regulated by keeping the uniform flow constant and gradually increasing the flow rate through port 2 (marked as a red circle). (b) and (c) show a test case, where the flow rate at the upstream inlet is 20 μl/min and at port 2 is 50 μl/min from the source-based panel method and experiment, respectively. The scale bar represents 4 mm.

A priori particle manipulation algorithm. We proceed by characterizing our particle manipulation approach and the computed *a priori* variations in the source/sink strengths. Numerically, the *a priori* particle manipulation algorithm is first assessed on an arbitrary test case. In this test case, two particles that are initially traveling on the same streamline are separated such that both reach an imposed final position for which the two particles are on separate streamlines. Figure 2(b) shows the particle trajectory of a particle pair when forced to travel on a pre-defined particle trajectory without first and second optimization steps. Figure 2(e) shows the particle trajectories calculated using the *a priori* particle manipulation algorithm, which is a two-step optimization routine. Figures 2(c) and 2(d) indicate that if two particles are traveling on a certain pre-defined particle trajectory, the required flow rates can be almost 15 times larger compared to the flow rates calculated from the *a priori* particle manipulation algorithm. Moreover, the *a priori* particle manipulation algorithm eliminates the sharp variations in the flow rate, which are seen in the flow rates of the non-optimized solution. A similar effect of the particle optimization routine was noticed by Schneider *et al.*[8] We verify that the computed optimal flow rates can be achieved and imposed in our experiments given the technical limitations of the flow controllers.

Figure 4 presents our results for an experiment where a particle follows a pre-computed optimized trajectory with minor deviations. We maintain a constant uniform flow of 80 μm/s (20 μl/min), causing the particle to approach the measurement domain along the X direction. We provide as an input the initial particle position $\boldsymbol{X}_{pi}(t_0)$ and final position $\boldsymbol{X}_{pi}(t_f)$, and the *a priori* particle manipulation algorithm computes an optimized trajectory with the corresponding flow rates, see Figs. 4(a) and 4(b). These are transmitted to the pump. Once the particle reaches the starting point, $\boldsymbol{X}_{pi}(t_0)$, the pre-computed flow rates are imposed without any feedback control and alter the streamline pattern in the flow cell to guide the particle toward its final position $\boldsymbol{X}_{pi}(t_f)$. The experimentally measured trajectory [dashed line in Fig. 4(a)] closely agrees with the simulated trajectory [solid line in Fig. 4(a)], with a maximum error of only 0.8% of the linear dimension of the measurement domain ($12 \times 12\,\text{mm}^2$). The precision of our approach lies in the close control of the volumetric flow rate, characterized by the pre-computed strength of source/sink in potential flow. The streamlines during the manipulation time of, t = 6, 36, and 74 s are plotted, corresponding to Figs. 4(c)–4(e), respectively. Throughout the manipulation event, the streamline pattern does not change significantly. Our Hele–Shaw geometry with inlet/outlet port design ensures excellent agreement between the streamlines computed using a reduced-base numerical potential flow solver and those recorded experimentally. It bears emphasis that in this example, no feedback control is implemented, and the precomputed input for the volumetric flow rates $[Q_1, Q_2, Q_3]$ through the ports is directly imposed. These results indicate that the flow cell design and the panel method numerical approach provide enough precision and that the particle manipulation do not require complex feedback control to reach high accuracy in the manipulation. In the following, we show that a simple PID controller is sufficient to correct any minor particle deviations for more complex manipulations.

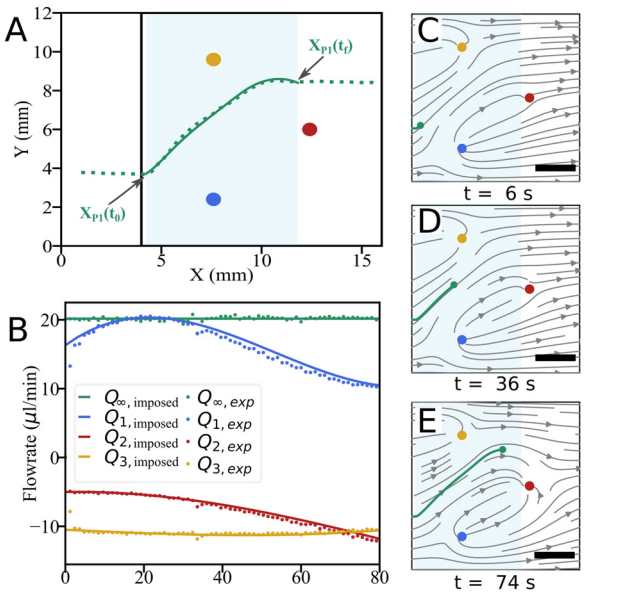

FIG. 4. Particle deflection: (a) Particle trajectories showing particle deflection for optimized particle trajectories (green solid line: particle 1) and experimentally measured (green dashed line: particle 1) data. $\boldsymbol{X}_{P1}(t_0)$ and $\boldsymbol{X}_{P1}(t_f)$ denote pre-defined initial and final particle locations for particle 1, respectively. The measurement domain is marked by the black square box. The blue shaded area marks the manipulation region. (b) Imposed and experimentally measured flow rates. The streamlines are computed from the flow rates recorded during the experiment at different time instants: (c) $t = 6$ s, (d) $t = 36$ s, and (e) $t = 74$ s. The circles represent inlet/output port 1 (filled blue circle), 2 (filled red circle), and 3 (filled yellow circle), respectively. The scale bar represents 4 mm.

Real-time control of particle manipulation. For more complex manipulations involving two particles, the experimentally obtained particle trajectory can deviate from the pre-computed trajectories. In practice, these deviations remain small and correcting for these can be achieved with a simple PID controller and does not require a more computationally expensive controlling approach, such as model predictive control. The coordinates of the particles are acquired during the experiment from the in-house developed image acquisition LabVIEW program. The initial and final particle locations, i.e., $\boldsymbol{X}_{pi}(t_0)$ and $\boldsymbol{X}_{pi}(t_f)$ respectively, are used as input parameters for the *a priori* particle manipulation algorithm written in Matlab. The Matlab program computes the optimized flow rate for the given particle manipulation, which is further transmitted to the LabVIEW program to deliver the required flow rates into the flow cell. Additionally, with the PID feedback loop in an experiment, the error in particle position can be determined with respect to the *a priori* optimized trajectory and additional flow rates can be given to correct for the error.

A single particle trap experiment is performed to determine the effectiveness of the PID controller in suppressing the particle position error between the experimentally measured particle position and the optimized particle trajectory. As the stagnation point is inherently unstable, the flow rates are adjusted to maintain the particle trapped in a position by giving small corrections to the flow rates. The strength of the flow rate correction is calculated using the particle position error between the experimentally measured particle position and the optimized particle trajectory.

In this case, a flow rate of 20 μl/min is imposed upstream and yields a uniform flow, $\mathbf{u} = (80, 0)$ μm/s. The particle approaches the measurement domain from the centerline along the width of the

device. The particle is trapped in the control area (red-shaded region) as shown in Fig. 5(a). Based on the initial particle position $\boldsymbol{X}_{P1}(t_0)$ and trapping location, the particle manipulation algorithm calculates the optimized particle trajectory and the corresponding flow rates are transmitted into the pump. As the particle enters the manipulation area, the pre-computed flow rates are imposed. The green dots in Fig. 5(a) indicate the experimentally measured particle position, which shows that the particle significantly slows down in the trapping area. During the experiment, the flow rate corrections reduce the error [Fig. 5(b) (inset)], as the particle positional error increases between t = 0 and 120 s [Fig. 5(c)]. The flow rate corrections modulate the pre-computed flow rate components such that the error is again within the threshold. Next, the streamlines are analyzed using the flow rates measured experimentally at the time, t = 100, 150, and 200 s corresponding to Figs. 5(d)–5(f), respectively. The particle starts to slow down as ports 1 and 3 act as sinks, and port 2 acts as a source [Fig. 5(d)] until the particle becomes trapped at the stagnation point. As the stagnation point is inherently unstable, the flow rates are adjusted to maintain the particle trapped in a position by giving small corrections to the flow rates [Fig. 5(e)]. Eventually, the particle resumes the downstream motion after the trapping time has passed [Fig. 5(f)]. Figure 5 shows selected frames from the experimental video for the single-particle trapping (multimedia view) and the corresponding streamline visualization (multimedia view), respectively.

In the trapping duration of 60 s, in Fig. 6(a), the experimentally determined particle position translates in the x direction by 390 μm between t = 50 s and 78 s. From t = 78 to 110 s, the particle is stagnant at the X-position of 6.40 mm. Throughout the experiment in the y direction, experimentally measured particle position had no significant deviation compared to the optimized particle trajectory; see Fig. 6(b).

Separating particle pair Here, the functionality of the micro-device is demonstrated for particle separation. This test case simulates a Y-channel where each particle flows in either of the two branches of the channel. Based on the pre-defined final positions $\boldsymbol{X}_{P1}(t_f)$ and $\boldsymbol{X}_{P2}(t_f)$ for particles 1 and 2, respectively, and their potential starting points, $\boldsymbol{X}_{P1}(t_0)$ and $\boldsymbol{X}_{P2}(t_0)$ where the particle pair would enter the square domain, optimized particle trajectories are computed using an *a priori* particle manipulation algorithm. The optimized particle trajectories (solid green and red lines) and the experimentally measured particle trajectories (dashed green and red lines) are indicated in Fig. 7(a). During the experiment, the feedback loop system computes the experimentally measured particle positional errors for the optimized trajectories and provides flow rate corrections accordingly. A good agreement between the imposed and the experimentally measured flow rates is shown in Fig. 7(b). Considerably lower flow rate corrections were required in this test case [Fig. 7(b) (inset)]. The particle positional error of particle 1 is within the threshold for the entire duration of the experiment, as shown in Fig. 7(c). The positional error of particle 2 falls outside the threshold for the majority of the manipulation duration; this might be due to the off-center particle position with respect to the channel height. During the experiment, when the normalized weight of particle 2 is increased with respect to that of particle 1, the positional error starts to decrease for particle 2 and to increase for particle 1, but remains within the threshold limit.

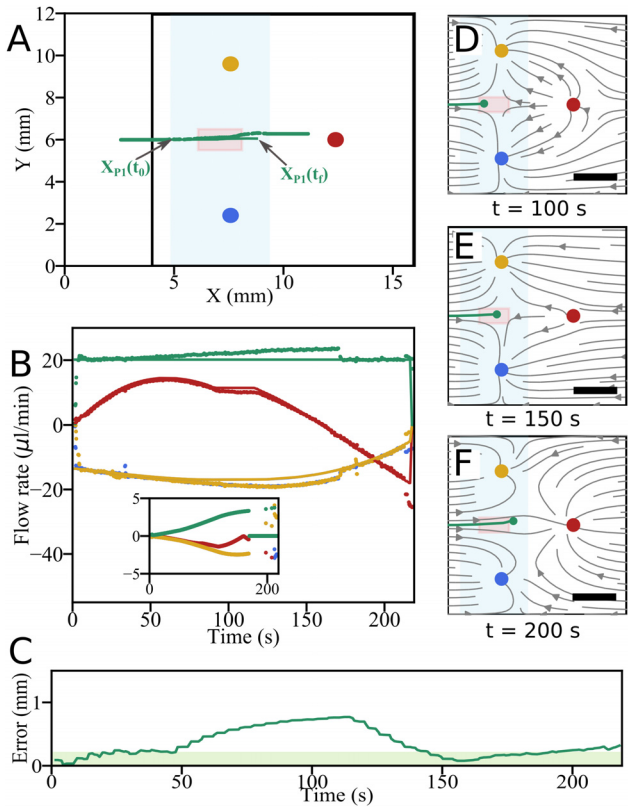

FIG. 5. (a) Particle trajectories showing particle trapping for green solid line: optimized particle trajectory and filled green circle: experimentally measured particle trajectory. $\boldsymbol{X}_{P1}(t_0)$ and $\boldsymbol{X}_{P1}(t_f)$ denotes pre-defined initial and final particle location for particle 1, respectively. The black square box marks the measurement domain. The blue shaded area indicates the manipulation region. The red shaded area shows the particle trapping location. The video of the actual experiment is available online, where the particle appears as a white dot on a black background. (b) Imposed and experimentally measured flow rates. (Inset) Flow rate corrections by PID controller to minimize the particle's positional error. (c) Positional error as a function of time. The green shaded area represents the mean particle diameter, 212 μm, considered as the acceptable threshold. The particle tracks are computed from the streamlines. The streamlines are computed from the flow rates recorded during the experiment at different time instants: (d) t = 100 s, (e) t = 150 s, and (f) t = 200 s. The circles represent inlet/outlet ports 1 (filled blue circle), 2 (filled red circle), and 3 (filled yellow circle). The scale bar represents 4 mm. A video shows the animation of the data included in A.-F. Multimedia available online.

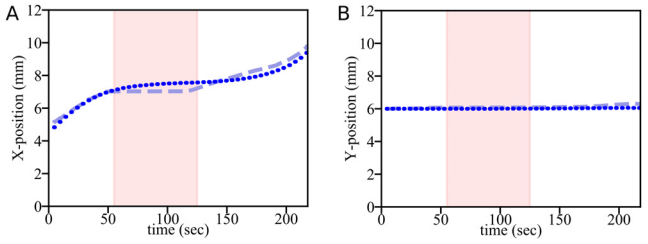

FIG. 6. The dashed lines shows the optimized particle trajectory and the dotted line shows the experimentally measured position for a particle that is trapped and released. The red shaded region shows the pre-defined particle trap duration. (a) Particle displacement in the X direction as a function of time. (b) Particle displacement in the Y direction as a function of time.

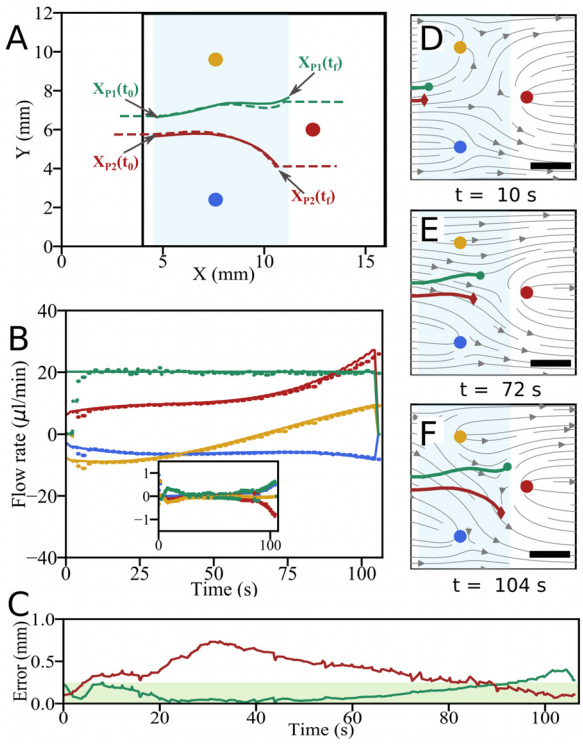

FIG. 7. Separating a particle pair: (a) Particle trajectories showing particle separation for optimized particle trajectories (green solid line: particle 1, red solid line: particle 2) and experimentally measured (green dashed line: particle 1, red dashed line: particle 2) data. $X_{P1}(t_0)$ and $X_{P1}(t_f)$ denote pre-defined initial and final particle locations for particle 1, respectively. Similarly, $X_{P2}(t_0)$ and $X_{P2}(t_f)$ are for particle 2. The measurement domain is marked by the black square box. The blue shaded area marks the manipulation region. The video of the actual experiment is available online, where the particle appears as a white dot on a black background. (b) Imposed and experimentally measured flow rates. (Inset) Flow rate corrections by PID controller during the experiment to minimize the positional errors of the particles. (c) Positional errors as a function of time for particle 1 (green solid line) and particle 2 (red solid line). The green shaded area indicates the mean particle diameter, 212 μm, which is considered as an acceptable threshold. The streamlines are computed from the flow rates recorded during the experiment at different times: (d) $t = 10$ s, (e) $t = 72$ s, and (f) $t = 104$ s. The circles represent inlet/output port 1 (filled blue circle), 2 (filled red circle), and 3 (filled yellow circle). The scale bar represents 4 mm. A video shows the animation of the data included in A.-F. Multimedia available online.

Furthermore, the streamline patterns are analyzed using the experimentally measured flow rates during the manipulation at times, $t = 10$, 72, and 104 s, corresponding to Figs. 7(d)–7(f), respectively. The particles continue to move downstream, with particle 1 moving toward port 3, which acts as a sink [Fig. 7(d)]. As the particles move downstream, they separate further as a result of port 1 acting as a sink, and the distance between the particles increases [Fig. 7(e)]. As the particles travel toward port 2, the source strength of the port 2 increases to separate the two particles and move them closer to their pre-defined final positions [Fig. 7(f)]. Figure 7 shows selected frames from the video of the experiment with the separation of a particle pair (multimedia view) and the corresponding streamline visualization (multimedia view), respectively.

Joining two particles Two particles were brought together to demonstrate the functionality of our flow cell for studies related to coalescence, particle assembly, and adhesion. The *a priori* manipulation algorithm determines the optimized particle trajectories and the corresponding flow rates from the desired initial and final particle positions. The optimized particle trajectories (solid green and red lines) and experimentally measured particle trajectories (dashed green and red lines) are indicated in Fig. 8(a). A maximum of 10% deviation between the imposed and the experimentally measured flow rates is shown in Fig. 8(b). A small flow rate correction at the time $t = 100$ s is required [Fig. 8(b) (inset)]. The particle positional error of particle 2 is within the error threshold for the entire experiment. In this case, the particle position error of particle 1 remains constant until $t = 70$ s and

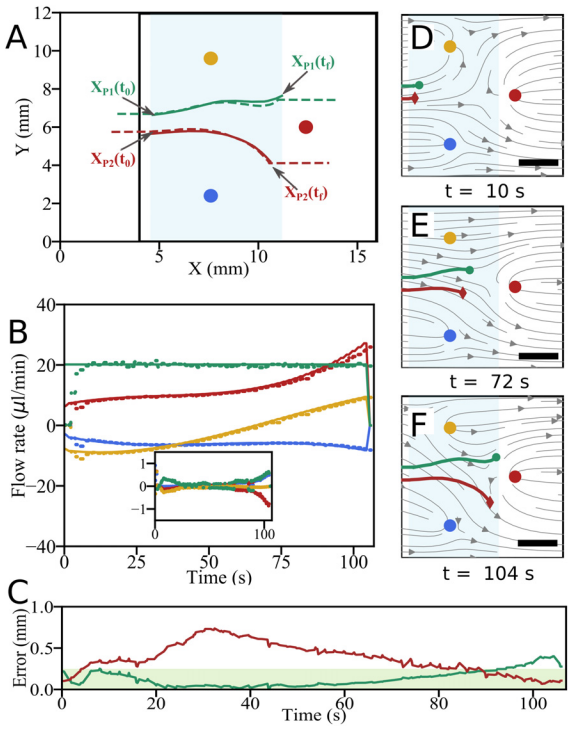

FIG. 8. Joining two particles: (a) Particle trajectories showing particles approaching each other for optimized particle trajectories (green solid line: particle 1, red solid line: particle 2) and experimentally measured (green dashed line: particle 1, red dashed line: particle 2) data. $X_{P1}(t_0)$ and $X_{P1}(t_f)$ denote pre-defined initial and final particle locations for particle 1, respectively. Similarly, $X_{P2}(t_0)$ and $X_{P2}(t_f)$ are for particle 2. The measurement domain is marked by the black square box. The blue shaded area indicates the manipulation region. The video of the actual experiment is available online, where the particle appears as a white dot on a black background. (b) Imposed and experimentally measured flow rates. (Inset) Flow rate corrections by PID controller during the experiment to minimize particle positional error. (c) Positional error as a function of time for particle 1 (green solid line) and particle 2 (red solid line). The green shaded area indicates the mean particle diameter, 212 μm, which is considered as an acceptable threshold. The particle tracks are computed from the streamlines. The streamlines are computed from the flow rates recorded during the experiment at different time instants: (d) $t = 16$ s, (e) $t = 55$ s, and (f) t $t = 75$ s. The circles represents inlet/output port 1 (filled blue circle), 2 (filled blue circle), and 3 (filled yellow circle), respectively. The scale bar represents 4 mm. A video shows the animation of the data included in A.-F. Multimedia available online.

increases for a short duration between $t = 70$ and 75 s. During the experiment, the normalized weight of particle 1 is increased with respect to particle 2, the particle position error for particle 1 decreases to the threshold level after that [Fig. 8(c)].

The streamline patterns determined using the experimentally measured flow rates show that both the particles move downstream, and particle 1 begins to move toward port 1 due to ports 1 and 2 acting as a source and sink, respectively, at the manipulation time, $t = 16$ s [Fig. 8(d)]. Both particles travel downstream, with particle 1 having a larger velocity due to a strong source and sink strengths from ports 1 and 2, respectively, forming a Rankine oval [Fig. 8(e)]. As the particles travel toward port 2, the sink strength of port 2 increases to move the two particles closer to each other to the pre-defined final particle position [Fig. 8(f)]; see Fig. 8 for selected frames from the video of the experiment with two particles coming close to each other (multimedia view) and the corresponding streamline visualization (multimedia view), respectively.

Virtual mixing channel This section demonstrates how we can switch the position of particles in a rectangular channel. In this experiment, there is a constant uniform flow, $\mathbf{u} = (40,0)$ μm/s which corresponds to a flow rate of 10 μl/min. The optimized particle trajectories (green and red solid lines) computed from the *a priori* particle manipulation algorithm correspond to switching the positions of two particles, where the particle initially moving along a streamline above the other is manipulated to move along a streamline underneath the other after the manipulation. The particle trajectories measured experimentally (dashed green and red lines) are also indicated in Fig. 9(a). In this experiment, a significant deviation arises between the imposed and the experimentally measured flow rates in the second half of the experiment, as shown in Fig. 9(b). Here, the flow rate corrections are substantial in the particle positional error [Fig. 9(b) (inset)]. Since the controller gains were kept constant, the high magnitude of the flow correction may be due to a small blockage in the inlet tubes or particles settling in the flow cell that reduces the velocity in the parabolic flow profile. This example shows that in practice the PID control is robust and can provide appropriate flow rate corrections to mitigate random disturbances in the experiment. The positional error of particle 2 increases significantly and might be due to the settling behavior of the particle in the flow cell. The flow rate corrections decreased the particle positional error to the threshold level [Fig. 9(c)].

Before the start of the manipulation activity, particle 2 is in front and below particle 1. At t = 68 s, both particles are close to each other near port 1 [Fig. 9(d)]. Both particles are subsequently deflected toward port 2, and particle 2 is pushed toward port 3 at a steep angle such that it moves on the other side of the trajectory of particle 1 [Fig. 9(e)]. Toward the end of the manipulation period, particle 2 is behind and above particle 1 [Fig. 9(f)]; see Fig. 9 for selected frames from the video of the experiment with two particles switching their position as they move downstream (multimedia view) and the corresponding streamline visualization (multimedia view).

Pollen trapping Our approach is general and not limited to one particular kind of particle. The flow is used as gentle tweezers to move particles within the flow cell, and the approach is particularly suited to biological samples. To demonstrate this, an arbitrary pollen grain is selected and trapped in the flow cell while the other pollen grains continue to flow. There has been considerable work done in pollen trapping.[30,31] Manipulation techniques such as electric or magnetic

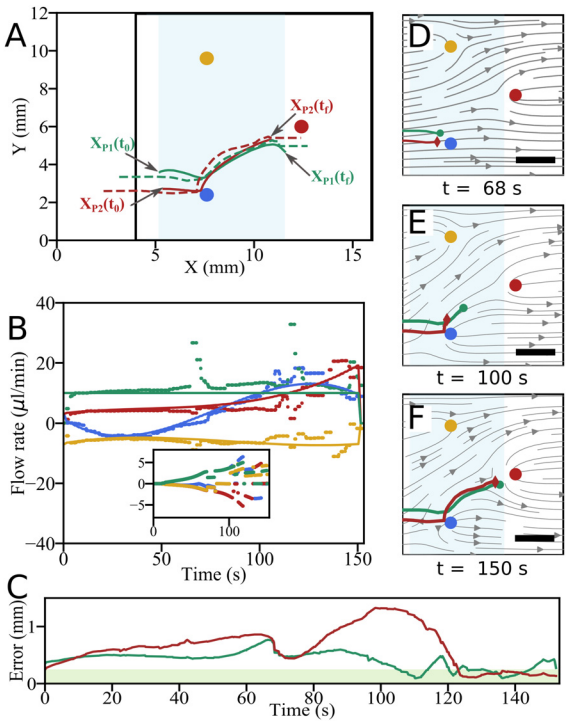

FIG. 9. Virtual mixing channel: (a) Particle trajectories showing particle mixing for optimized particle trajectories (green solid line: particle 1, red solid line: particle 2) and experimentally measured (green dashed line: particle 1, red dashed line: particle 2) data. $\boldsymbol{X}_{P1}(t_0)$ and $\boldsymbol{X}_{P1}(t_f)$ denote pre-defined initial and final particle locations for particle 1, respectively. Similarly, $\boldsymbol{X}_{P2}(t_0)$ and $\boldsymbol{X}_{P2}(t_f)$ are for particle 2. The black square box marks the measurement domain. The blue shaded area indicates the manipulation region. The video of the actual experiment is available online, where the particle appears as a white dot on a black background. (b) Imposed and experimentally measured flow rates. (Inset) Flow rate corrections by PID controller during the experiment. (c) Positional error for particle 1 (green solid line) and particle 2 (red solid line). The green shaded area indicates the threshold, corresponding to the particle diameter: 212 μm. The particle tracks are computed from the streamlines. The streamlines are computed from the flow rates recorded during the experiment at different time instants: (d) $t = 68$ s, (e) $t = 100$ s, and (f) $t = 150$ s. The circles represent inlet/output ports 1 (filled blue circle), 2 (filled red circle), and 3 (filled yellow circle), respectively. The scale bar represents 4 mm. A video shows the animation of the data included in A.-F. Multimedia available online.

manipulation are not feasible here. They do not create appropriate growth conditions for growing pollen tubes from a pollen grain, which promptly respond to chemical or electrical stimuli. The pollen trapping experiment is done in a similar manner as the particle trapping experiment explained previously. The experimental setup was modified for the pollen grain experiment by adding an additional camera for visualization. Furthermore, details on the pollen grain experimental setup are given in (Ref. 23, Sec. 4.2). The pollen grain approaches the measurement domain from the centerline along the width of the device. The objective is to trap the pollen at the stagnation point in the trapping area (red-shaded region) as shown in Fig. 10(a). As the pollen grain enters the manipulation region, significant flow rate corrections are required [Fig. 10(b) (inset)]. The magnitude of the corrections is of the same order as the pre-computed flow rates. The pollen diameter (70 μm) is significantly smaller than the channel height (350 μm).

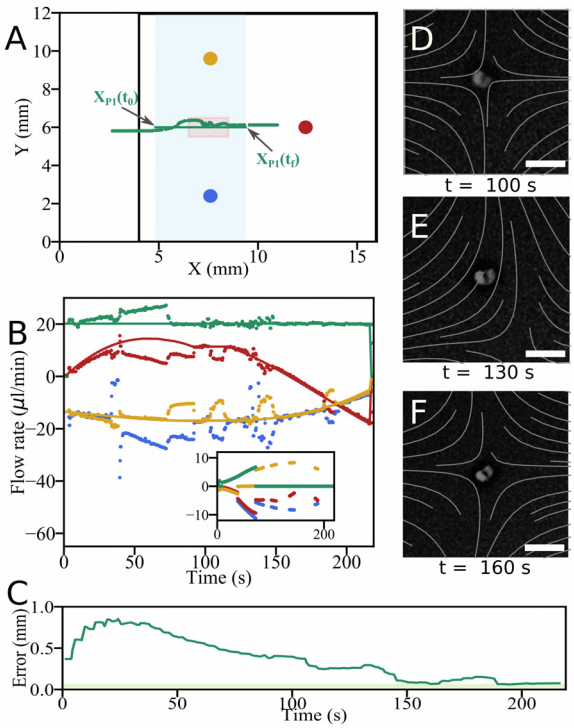

FIG. 10. Real-time pollen selection and trapping: (a) Particle trajectories showing pollen grain trapping for simulated (green solid line) and experiment (green dashed line) data. $\boldsymbol{X}_{P1}(t_0)$ and $\boldsymbol{X}_{P1}(t_f)$ denote pre-defined initial and final locations for the selected pollen grain, respectively. The black square box marks the measurement domain. The blue shaded area indicates the manipulation region. The red shaded area shows the particle trapping location. The video of the actual experiment is available online, where the particle appears as a white dot on a black background. (b) Imposed and experimentally determined flow rates. (Inset) Flow rate corrections by PID controller to minimize the positional error. (c) Positional error as a function of time. The green shaded area represents the mean pollen diameter, i.e., 70 μm, considered as the acceptable threshold. In this case, images of trapped pollen are shown at different time instants during the manipulation process: (d) $t = 100$ s, (e) $t = 130$ s, and (f) $t = 160$ s. The gray lines depict the streamlines around the pollen grain. The circles represent inlet/output ports 1 (filled blue circle), 2 (filled red circle), and 3 (filled yellow circle), respectively. The scale bar represents 250 μm. A video shows the animation of the data included in A.-F. Multimedia available online.

Thus, the probability of the pollen grain not being at the centerline along the channel height is significant. At the start of the experiment, the positional error is large and gradually decreases throughout the experiment to the threshold value of 70 μm, corresponding to the pollen grain diameter. Figures 10(d)–10(f) correspond to pollen grain trapping at the manipulation time of 100, 130, and 160 s, respectively, as seen with a 3 × zoom lens along with the streamline imposed from the experimental flow rate data. The streamlines vary with time to keep the pollen grain at the same position; see Fig. 10 (multimedia view) for the pollen trapping experiment as seen by an 1 × lens (for pollen manipulation) and 3 × zoom lens (for visualization).

IV. DISCUSSION AND CONCLUSION

This article describes a method to create "virtual channels" in a Hele–Shaw cell using only hydrodynamic forcing. The flow model is validated by comparing the position of a stagnation point induced by a single source in a uniform flow. The model for the bulk fluid velocity and the particle velocity is based on the assumption that the depth-averaged flow in the Hele–Shaw cell behaves as a potential flow. This assumption allows us to take a linear superposition of 2D point sources and uniform flow to represent and compute the flow patterns. Figure 3 demonstrates that the spatial position of the stagnation point induced by varying the source strength, predicted by the source-based panel method and COMSOL simulations, are in agreement with the experimental data. A key advantage of the panel method is that it is based on potential flow theory, making it computationally far less expensive than COMSOL simulations, which is beneficial for real-time applications.

A novel *a priori* particle manipulation algorithm is introduced to determine optimal particle trajectories, based on the pre-defined initial and final particle location. The optimized particle trajectory is calculated by minimizing both the magnitude and the time variations of the flow rates. The *a priori* particle manipulation algorithm can be scaled to different Hele–Shaw cells based on their physical dimensions. This is possible because all optimization calculations are performed using non-dimensional terms, scaled by the length scale of the region of interest, channel height, and the uniform flow velocity. The five inlet/outlet ports in the current flow cell correspond to the minimum number of ports required to manipulate two particles simultaneously. These five ports are designed to include one inlet for uniform flow, three ports for liquid injection or extraction, and an outlet to ensure mass conservation.

However, some factors are not included in the *a priori* computations, such as particle density and off-center particle position along the channel height. Hence, to enhance the repeatability of the experiments, a feedback loop is necessary. This is achieved by implementing a PID control system, which uses the pre-computed optimized trajectories from the *a priori* particle manipulation algorithm. The linear nature of potential flow simplifies and speeds up the control strategy. The PID controller provides flow rate corrections, added to the pre-computed flow rates, based on real-time measurements of particle deviation from the pre-computed optimized particle trajectories.

With this PID control strategy, the flow cell can replicate various fundamental microfluidic processes such as trapping (see Fig. 10), sorting, separating (see Fig. 7), joining (see Fig. 8), and interchanging (see Fig. 9). This system can be used in chemical and biological processes such as cell trapping, cell interactions, cell separations, micro-reactors, particle assembly, adhesion, droplet coalescence, and mixing. A potential application of this device was demonstrated by trapping an arbitrary pollen grain in the flow cell (see Fig. 10), for 60 s, while other pollen grains where advected by the flow. In principle, the trapping time can be adjusted based on the user requirements. A key advantage of using hydrodynamic forcing is that it avoids external influences, such as electric or acoustic fields, which could otherwise affect chemical or biological samples.

In the future, adding more ports could make the system for two-particle manipulation more redundant. Increasing the number of inlet/outlet ports would also contribute to improving the stability of streamlines. Moreover, coupling the *a priori* particle manipulation algorithm with a more robust feedback loop such as non-linear model predictive control (NMPC) could further improve particle manipulation. NMPC could be applied with a pre-determined time horizon since the most stable optimized particle trajectories are computed from the *a priori*

particle manipulation algorithm. Additionally, an adaptive feedback controller could be developed to dynamically select controller parameters based on the particle locations and the pre-computed flow rates. Furthermore, optimization could also be performed to identify the ideal locations and configurations for the inlet/outlet ports, minimizing both absolute flow rates and flow rate variations.

SUPPLEMENTARY MATERIAL

See the supplementary material for detailed information on the experimental characterization of the pump response time and the working principle of the PID controller, including a high-level flow chart illustrating the experimental sequence using the *a priori* particle manipulation algorithm with a PID feedback controller.

ACKNOWLEDGMENTS

This research was supported by Shell Technology Centre Amsterdam (STCA), the Netherlands, and Shell Global Solutions International B.V., the Netherlands (Grant No. PT66562). The authors are thankful to Dr. H. Burak Eral for access to use his laboratory facilities to fabricate the microfluidic devices. Furthermore, Antaran Deka and Kalpit Bakal contributed to this work.

AUTHOR DECLARATIONS

Conflict of Interest

The authors have no conflicts to disclose.

Author Contributions

Ankur Kislaya: Conceptualization (equal); Data curation (equal); Formal analysis (equal); Methodology (equal); Software (equal); Validation (equal); Visualization (equal); Writing – original draft (equal). **Aniket Ashwin Samant:** Methodology (equal); Software (equal); Writing – review & editing (equal). **Peter Veenstra:** Funding acquisition (equal); Methodology (equal); Supervision (equal). **Daniel S. W. Tam:** Conceptualization (equal); Formal analysis (equal); Methodology (equal); Supervision (equal); Writing – review & editing (equal). **Jerry Westerweel:** Conceptualization (equal); Formal analysis (equal); Funding acquisition (lead); Methodology (equal); Supervision (equal); Writing – review & editing (equal).

DATA AVAILABILITY

The data that support the findings of this study are available within the article and its supplementary material.

REFERENCES

[1]A. Karimi, S. Yazdi, and A. M. Ardekani, "Hydrodynamic mechanisms of cell and particle trapping in microfluidics," Biomicrofluidics **7**, 1–23 (2013).
[2]P. Sajeesh and A. K. Sen, "Particle separation and sorting in microfluidic devices: A review," Microfluid. Nanofluid. **17**(1), 1–52 (2014).
[3]C. Wyatt Shields, IV, C. D. Reyes, and G. P. López, "Microfluidic cell sorting: A review of the advances in the separation of cells from debulking to rare cell isolation," Lab Chip **15**(5), 1230–1249 (2015).
[4]A. M. Pit, M. H. G. Duits, and F. Mugele, "Droplet manipulations in two phase flow microfluidics," Micromachines **6**(11), 1768–1793 (2015).
[5]S. Zhang, Y. Wang, P. Onck, and J. den Toonder, "A concise review of microfluidic particle manipulation methods," Microfluid. Nanofluid. **24**(4), 1–20 (2020).
[6]W. Zhang, Z.-H. Shi, W.-F. Li, H.-F. Liu, and F.-C. Wang, "Particle clusters within inertial vortical flows in micro-cross-shaped channels," Phys. Fluids **34**(11), 112006 (2022).
[7]A. T. Brimmo and M. A. Qasaimeh, "Stagnation point flows in analytical chemistry and life sciences," RSC Adv. **7**(81), 51206–51232 (2017).
[8]T. M. Schneider, S. Mandre, and M. P. Brenner, "Algorithm for a microfluidic assembly line," Phys. Rev. Lett. **106**(9), 094503 (2011).
[9]M. Tanyeri, E. M. Johnson-Chavarria, and C. M. Schroeder, "Hydrodynamic trap for single particles and cells," Appl. Phys. Lett. **96**(22), 224101 (2010).
[10]M. Tanyeri, M. Ranka, N. Sittipolkul, and C. M. Schroeder, "A microfluidic-based hydrodynamic trap: Design and implementation," Lab Chip **11**(10), 1786–1794 (2011).
[11]M. Tanyeri and C. M. Schroeder, "Manipulation and confinement of single particles using fluid flow," Nano Lett. **13**(6), 2357–2364 (2013).
[12]A. Shenoy, M. Tanyeri, and C. M. Schroeder, "Characterizing the performance of the hydrodynamic trap using a control-based approach," Microfluid. Nanofluid. **18**, 1055–1066 (2015).
[13]A. Shenoy, C. V. Rao, and C. M. Schroeder, "Stokes trap for multiplexed particle manipulation and assembly using fluidics," Proc. Natl. Acad. Sci. U. S. A. **113**, 3976–3981 (2016).
[14]A. Shenoy, D. Kumar, S. Hilgenfeldt, and C. M. Schroeder, "Flow topology during multiplexed particle manipulation using a stokes trap," Phys. Rev. Appl. **12**(5), 054010 (2019).
[15]D. Kumar, A. Shenoy, S. Li, and C. M. Schroeder, "Orientation control and nonlinear trajectory tracking of colloidal particles using microfluidics," Phys. Rev. Fluids **4**(11), 114203 (2019).
[16]D. P. Taylor and G. V. Kaigala, "Reconfigurable microfluidics: Real-time shaping of virtual channels through hydrodynamic forces," Lab Chip **20**(10), 1720–1728 (2020).
[17]D. P. Taylor, P. Mathur, P. Renaud, and G. V. Kaigala, "Microscale hydrodynamic confinements: Shaping liquids across length scales as a toolbox in life sciences," Lab Chip **22**, 1415–1437 (2022).
[18]F. Paratore, V. Bacheva, M. Bercovici, and G. V. Kaigala, "Reconfigurable microfluidics," Nat. Rev. Chem. **6**(1), 70–80 (2021).
[19]B. R. Lutz, J. Chen, and D. T. Schwartz, "Hydrodynamic tweezers: 1. Noncontact trapping of single cells using steady streaming microeddies," Anal. Chem. **78**(15), 5429–5435 (2006).
[20]F. Storti, S. Bonfadini, and L. Criante, "Simplified 3D hydrodynamic flow focusing for lab-on-chip single particle study," Sci. Rep. **13**, 14671 (2023).
[21]Y. Song, Y. Zhou, K. Zhang, Z. Fan, F. Zhang, and M. Wei, "Microfluidic programmable strategies for channels and flow," Lab Chip **24**, 4483–4513 (2024).
[22]R. Garmasukis, C. Hackl, A. Charvat, S. G. Mayr, and B. Abel, "Rapid prototyping of microfluidic chips enabling controlled biotechnology applications in microspace," Curr. Opin. Biotechnol. **81**, 102948 (2023).
[23]A. Kislaya, "Particle manipulation-on-chip," Ph.D. thesis (Technische Universiteit Delft, 2022).
[24]G. K. Batchelor, *An Introduction to Fluid Dynamics* (Cambridge Mathematical Library, Cambridge University Press, 2000).
[25]P. K. Kundu, I. M. Cohen, and D. R. Dowling, *Fluid Mechanics* (Elsevier, 2012).
[26]J. Katz and A. Plotkin, *Low-Speed Aerodynamics*, Cambridge aerospace series, 2nd ed. (Cambridge University Press, 2001).
[27]C. Pozrikidis, "The motion of particles in the Hele-Shaw cell," J. Fluid Mech. **261**, 199–222 (1994).
[28]C. G. Broyden, "The convergence of a class of double-rank minimization algorithms 1. General considerations," IMA J. Appl. Math. **6**(1), 76–90 (1970).
[29]A. Kislaya, A. Deka, P. Veenstra, D. S. W. Tam, and J. Westerweel, "Psi-PIV: A novel framework to study unsteady microfluidic flow," Exp. Fluids **61**, 1–15 (2020).
[30]M. Ghanbari, A. Nezhad, C. Agudelo, M. Packirisamy, and A. Geitmann, "Microfluidic positioning of pollen grains in lab-on-a-chip for single cell analysis," J. Biosci. Bioeng. **117**(4), 504–511 (2014).
[31]A. S. Kashani and M. Packirisamy, "Efficient low shear flow-based trapping of biological entities," Sci. Rep. **9**(5511), 1–15 (2019).